CrossMark

ORIGINAL

Numerical and experimental investigation of turbine blade film cooling

Amar Berkache[1] · Rabah Dizene[1]

Abstract The blades in a gas turbine engine are exposed to extreme temperature levels that exceed the melting temperature of the material. Therefore, efficient cooling is a requirement for high performance of the gas turbine engine. The present study investigates film cooling by means of 3D numerical simulations using a commercial code: Fluent. Three numerical models, namely k-ε, RSM and SST turbulence models; are applied and then prediction results are compared to experimental measurements conducted by PIV technique. The experimental model realized in the ENSEMA laboratory uses a flat plate with several rows of staggered holes. The performance of the injected flow into the mainstream is analyzed. The comparison shows that the RANS closure models improve the over-predictions of center-line film cooling velocities that is caused by the limitations of the RANS method due to its isotropy eddy diffusivity.

Nomenclature

x, y, z	Cartesian coordinates (mm)
U	Axial velocity component (m.s^{-1})
V	Vertical velocity component (m.s^{-1})
T	Temperature (°C)
y$^+$	Dimensionless value of y (mm)
U$_e$	Crossflow inlet velocity (m.s^{-1})
U$_i$	Injection flow velocity (m.s^{-1})
D	Diameter of the jet hole (mm)
K	Turbulent kinetic energy (m^2.s^{-2})

M	Blowing ratio
α	Jet angle inclination (°)
δ	Boundary layer thickness (mm)
μ$_t$	Eddy viscosity
ω	Dissipation frequency rate (s^{-1})
u*	Friction velocity (m.s^{-1})
τ$_w$	Wall shear stress (kg.m.s^{-2})
ρ$_e$	Injection density flow (kg.m^{-3})
ρ$_i$	Main density flow (kg.m^{-3})
ε	Turbulent energy dissipation (m^2.s^{-3})

✉ Amar Berkache
   omar_berkache@yahoo.fr

[1] Energy Mechanics and Conversion Laboratory (LMESC), Mechanical Engineering Department, USTHB University, 32, El Alia, 16111 Bab Ezzouar, Algiers, Algeria

1 Introduction

The need for higher overall efficiency and higher specific thrust in flying or landing requires high gas turbine entry temperatures and turbine components are subjected to high thermal stresses. This place severe demands on the components which work in high temperature environment, such as turbine rotors and vanes. The turbine blades cannot withstand these temperatures. Consequently, cooling of gas turbine components is inevitable, and film cooling is widely used as an effective means to maintain component temperatures at acceptable levels. In an attempt to improve the film cooling performance, attention has been paid to some geometric parameters as the whole geometry contour and recently several staggered rows of jets. Investigations on film cooling performance of compound angle shaped holes also can be found as another geometric parameter and have an effect on cooling performance. Generally, compound angle shaped holes produce higher effectiveness and better protection over much wider ranges of blowing ratio than the axially oriented holes.

Cooling of a gas turbine blade was one of the most important problem which was targeted by different researchers in

the past. The combination of impingement cooling, convection cooling and film cooling is now considered as the most efficient way of cooling a turbine blade, using air drawn off the compressor. The air coming from the compressor is introduced into the turbine blades by their roots, allowing also cooling other components like the edge of the turbine disc or the turbine casing. There are three major cooling processes: cooling by forced convection, transpiration cooling and cooling by protective film. In the case of forced convection, the blade cooling is ensured by the heat exchange between the hot gas on the outer side of the blade and the fresh gas flowing inside the blade and rejecting heat at the trailing edge. Spraying air from the inner tubes cools the leading edge. In the case of transpiration cooling, the air is forced through the porous walls of the blade. This cooling system allows good thermal performance with very efficient cooling. Nevertheless, current materials and manufacturing problems with the constraint of high performance justify the impossible application of this type of system in turbine blades. In the third technique, film cooling is used to protect the outer wall of the blade. The cold air is extracted from the internal channels of the blade and it is injected outside the leading edge. It creates a thin cold film protecting the blade surface from hot gas. The protective film can be obtained by three methods: i) direct injection of the air in various locations along the suction surface, ii) uniform injection with a continuous film over the surface of the blade, and iii) transpiration cooling. Currently; cooling by protective film is the best type comparing to the others, which gives the best results.

The literature survey shows that a considerable effort has been devoted to understand the coolant film performance and its interaction with the mainstream flow. The film cooling performance is influenced by many parameters such as the wall curvature, the three-dimensional external flow structure, the free-stream turbulence, the blowing ratio, the compressibility, the flow unsteadiness, the whole size, shape and location, and the injection angle. Both the experimental investigations and the numerical simulations were carried out to analyze the performance of film cooling. CFD analysis is a powerful tool to obtain detailed data on the flow structure and heat transfer in a turbine cascade that are necessary to design and optimize a gas turbine. However, a systematic work has to be performed in order to validate the CFD model including selection of the turbulence model, specifying adequate inlet conditions, evaluation of the grid dependence, etc. At that, among other data of practical interest, the local heat transfer is most sensitive to peculiarities of secondary flows and, consequently, to details of physical and computational modelling.

Experimental measurements are available for the flat plate at many axial locations for given Mach number, Reynolds number, turbulence intensity at the leading edge. Thus, from the simulation point of view, the most popular turbulence models utilized for flow and heat transfer calculations are

the high and low Reynolds numbers two-equation eddy viscosity models, k-ε and k-ω. These models often provide a good balance between complexity and accuracy. Their ability to predict transition to turbulence; which is often present on turbine blades, and to integrate to the walls, are other reasons for their wide use. The majority of the reported film cooling simulation studies are based on the time averaged (RANS) equations. Experimental studies of Andreopolous and Rodi, [1], Fric and Roshko, [2] and Dizene et al., [3] have revealed that the near field of the jet is highly complex, three dimensional characterized by large scale coherent structures in the form of jet shear layer vortices which dominate the initial portion of the jet, the horseshoe vortex wrapping around the base of the jet, the counter rotating vortex pair which results from the impulse of the cross flow on the jet and dominate the turbulence structure in formed mixing layer. So, strong distortions in jet section resulted from the counter rotating vortex effects, and the wake vortices formed in the jet wake. The overview of the complex flow field produced by the interaction of the jet and cross flow is showed in Fig. 1. Ince and Leschziner [4] carried out an investigation using a high Reynolds RST model employing wall functions in order to avoid solving the Reynolds stresses all the way to the wall. Demuren [5] also reported predictions with a high-Re model using a multigrid method and obtained fairly good prediction of mean flow trends. The effects of the inclination of the holes on film cooling heat transfer coefficient have been studied by Sen et al. [6]. An additional study conducted by Schmidt et al. [7], reported on the effect of the angle on the adiabatic efficiency. Cho et al. [8] examined the orientation of the inclination of the hole and its influence on film cooling. They claimed that the injection ports laterally inclined produce cooling holes better than facing forward. Not only the shape but also the inclination of the holes can alter the performance of film cooling. Yuen and Martinez-Botas [9] measured the adiabatic efficiency through the liquid crystal thermography. They studied the influence of the injection ratio and orientation downstream of the inclination angle on efficiency. Three angles (30°, 60° and 90°) were tested. The angle of 30° gave the best cooling results. Gritsch et al. [10] in their paper presented detailed measurements of the film-cooling effectiveness for three single, scaled-up film-cooling hole geometries. The whole geometries investigated include a cylindrical hole and two holes with a diffuser-shaped exit portion. As compared to the cylindrical hole, both expanded holes show significantly improved thermal protection of the surface downstream of the ejection location, particularly at high blowing ratios. The predictions of several Reynolds-Averaged Navier-Stokes solutions for a baseline film cooling geometry are analyzed and compared with experimental data. There have been a number of studies that have utilized LES for film cooling. Tyagi and Acharya [11] performed LES of film cooling with a discretization scheme that is fourth-order accurate in space

Fig. 1 Flow diagram of a row of jets based on experimental results (R. Dizene et al.)
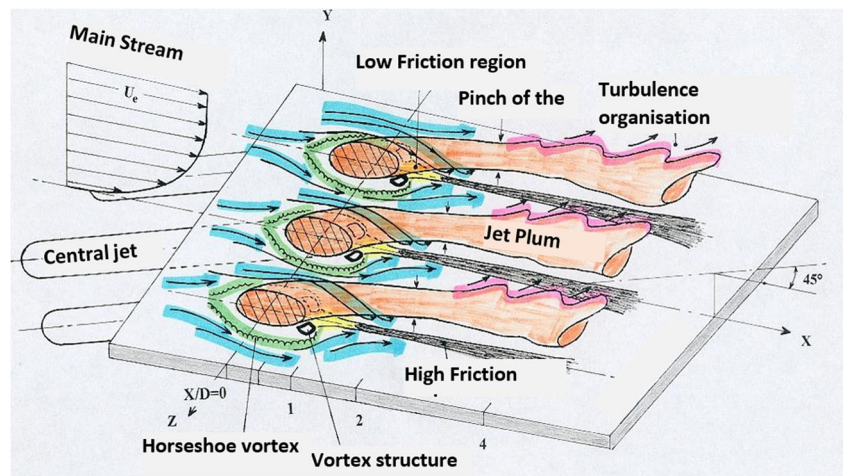
and third-order accurate in time and uses a dynamic mixed model for the computation of sub grid stresses. Inlet conditions from a RANS calculation are used at the bottom of the flow domain in the plenum, and a random perturbation generator is used to generate the turbulence for the delivery tube inlet. Predictions show the evolution of the flow structures and the role they play in the near-wall surface effectiveness. The LES study of Guo et al. [12] performed the flow field induced by the interaction between a single jet flow exhausting from a pipe and a turbulent flat plate boundary layer at a local Reynolds number of $Re_\infty = 400, 000$. The ratio R of the jet velocity to the cross-stream velocity is 0,1.

The flow regime investigated corresponds to that of gas turbine blade film cooling. In order to provide the realistic time-dependent turbulent inflow information for the crossflow, a LES of a spatially developing turbulent boundary layer is simultaneously performed using a rescaling method for compressible flow. The main flow features such as the separation area inside the pipe and the recirculation downstream of the jet exit are analyzed. The flow fields are examined in detail, but not compared to any other studies. David Houston Leedom [13] in a very recent study have performed LES for cylindrical holes with L/D ratios of 1,75 and 3,5 using a dynamic Smagorinsky model and no free stream turbulence. They have performed these simulations for a blowing ratio M of 0,5 to 2, and density ratio of 2. Yu Yaoa et al. [14] performed a Large Eddy Simulation (LES) of a high blowing ratio (M = 1.7) film cooling flow with density ratio of unity. Mean results are compared with experimental data to show the degree of reliability achieved in the simulation. Balaji et al. [15] presented, in their paper, the cooling effect of provision of pins of two different diameters and heights over the aircraft turbine blade tip at the corners.

The combination of film cooling and forced convection cooling still remains a current issue on the topic of turbine blade cooling. Therefore, the objective of the present study is the investigation of the dynamic interaction of multi-row

jets with the main flow simulating the expansion gases in the turbine. The first stages of the stator in a gas turbine subjected to high temperatures are simulated in the experimental apparatus. The geometrical configuration greatly affects heat exchange and cooling efficiency. In the present study, we apply three turbulence models to four inclined rows of jets in a cross flow. Numerical predictions are compared with the experimental data obtained using the PIV technique. In order to evaluate the predictive performances of each of the numerical models, the standard linear k-ε model, the RSM and the SST models are applied. The models have therefore been selected with the aim of isolating the influence of these terms on the interaction study and observing the behavior of the RANS modeling strategy used in this paper.

Numerical analysis has been carried out by Madhurima et al. [16], to find the film cooling effectiveness (centreline and spatially averaged). Variation of film cooling effectiveness has been determined along the downstream of cooling holes. The computational model has been validated with benchmark experimental literature. The study compares film cooling effectiveness over various blowing ratios (M), various hole shapes and rearrangement of holes. FLUENT solver has been used for the computational analysis using the standard RANS shear stress transport turbulence model. Computational results reveal that the effectiveness increases with increase in blowing ratios. On the other hand, film cooling effectiveness decreases due to coolant jet lift off and due to intermixing of coolant and mainstream flow. The best results were obtained for fan-shaped holes with blowing ratio (M) = 0,60. Spatially averaged effectiveness for fan-shaped holes was found to be higher as compared to other hole shapes.

Xiaokai Sun and Wei Peng [17] present a numerical investigation of 'The effect of holes shape on film cooling'. The results showed film cooling effectiveness is higher at the blowing ratio M = 0,5 for cylindrical hole; while for the hole with sister holes, film cooling performance is better at corresponding blowing ratio M = 1,0 and it is better than that of the

cylindrical hole. The reason is that the interaction between the mainstream and the cooling stream produces the counter-rotating vortex pairs (CVP) at high blowing ratio, which will make the hot mainstream underneath the cooling stream and lifts the cooling stream from the surface for the cylindrical hole. And the three cases of holes with sister holes can weaken the effect of the CVP.

The larger scales are anisotropic in nature, and are not well-represented by universal models. In view of this, the present work estimates the accuracy of film cooling dynamics prediction. Most calculations have been reported by solving the Reynolds-Averaged Navier-Stokes Equations (RANS) that require a turbulence model and compared with the experiments. With this approach, we estimate how the model may represent the effect of the fluctuations over the entire range of scales and their ability to resolve any part of the turbulent spectrum which must therefore be modeled. On the other hand, the advances in processor speed and parallel computing have made computer-intensive calculations possible, and solve the steady Navier-Stokes equations with sufficiently fine mesh-spacing.

2 Problem statement

Although experimental tests of a primary air flow crossed by a secondary flow on a flat wall with multiple holes were performed. The basic aim of these proposed geometries is to allow more uniform spreading of the jet along the surface resulting in uniform higher cooling. The experimental measurements have been conducted in the ISAE-ENSMA tunnel facility at the P′ institute in Poitiers (France), using a flat plate with several staggered rows of holes. Figures 2 and 3 show the ISAE-ENSMA tunnel facility and the positions of several staggered rows of 81 cylindrical cooling holes inclined at 30° from the wall with a 6 mm diameter of each one with elliptical edge ends whose value of the major diameter is equal to 12 mm. Figure 4 shows the geometrical distribution of the holes. Both mean and fluctuation velocity field measurements are realized using P.I.V. system. A double-pulsed Nd-Yag LASER (Quantel Big Sky) is used to set up the light sheet of the P.I.V. setup. The exit energy is nearly 20 mJ for each LASER pulse. The wavelength is 532 nm. The laser beams are focused onto a sheet by one cylindrical (f = −0,02 m) and one spherical (f = 0,5 m) lens. The time delay between two pulses, which depends on the velocity and the size of the observation fields, varies from 20 to 50 μs. The video images are recorded with a Hi-Sense Dantec camera. The frame grabber, using a pixel clock, digitizes the analogue video signal to an accuracy of 8 bits. In the frame grabber, each field is digitized in 1280*1024 pixels with gray levels. The acquisition frequency is 4 Hz. Interrogation of the recorded images is performed by two-dimensional digital cross correlation analysis using
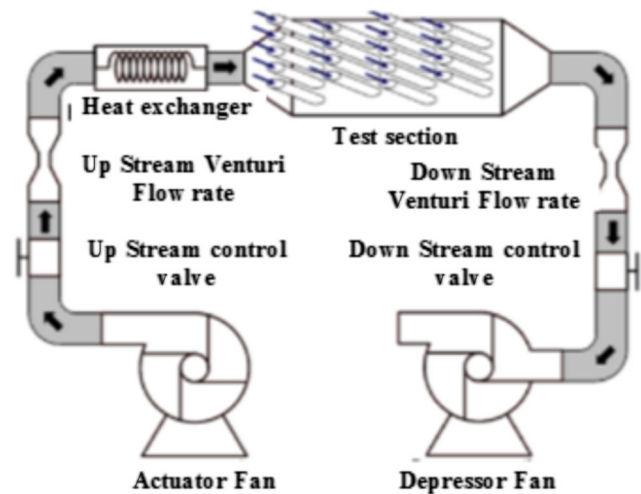

Fig. 2 General description of the tunnel facility

"Flow Manager". The final window has a size of 16 by 16 pixels (0,592 by 0,592 mm) and there is a 50% overlap. The flows are seeded with smoke generator.

A previous study of the drop size distribution has shown that the mean diameter is equal to 5 μm. For each velocity field, 300 P.I.V. images have been recorded. We had used these 300 velocity fields to calculate the different parameters such as mean velocity and velocity variance fields. A computation of the convergence of the first two moments of the velocity shows that 300 velocity fields are sufficient. Our PIV measurements are conducted using a flat plate crossed by four open rows of coolant jets with a fixed value of the blowing rate of M = 2 in reference with the ENSMA test facility, and inclined of 30 degrees relatively to the axial direction as shown in Fig. 5. The main and injection flows are located in the (x, y) plane. Experiments are made using a flat plate divided into 6 shooting planes. The camera can move in the plane (x, z) along the z-axis with a displacement of 35 mm between each plane. The Fig. 6 illustrates the six measure planes on the test facility. The experimental results obtained are used to validate the numerical results obtained by RANS simulation, conducted in the same conditions and using k-ε, RSM and Shear Stress Transport (SST) turbulence models in order to check which model gives the best prediction results in comparison with experience. The main flow is the movement in the x direction with a linear velocity equal to 2 m/s. While the direction of flow of the injection air is in a direction inclined at an angle of 30 ° relative to the x axis in the plane (x, z).

3 Experimental aparratus and protocol

To understand the influence of a secondary flow on a main flow in the cooling phenomenon of gas turbine

Fig. 3 General description of the test vein and the flat plate
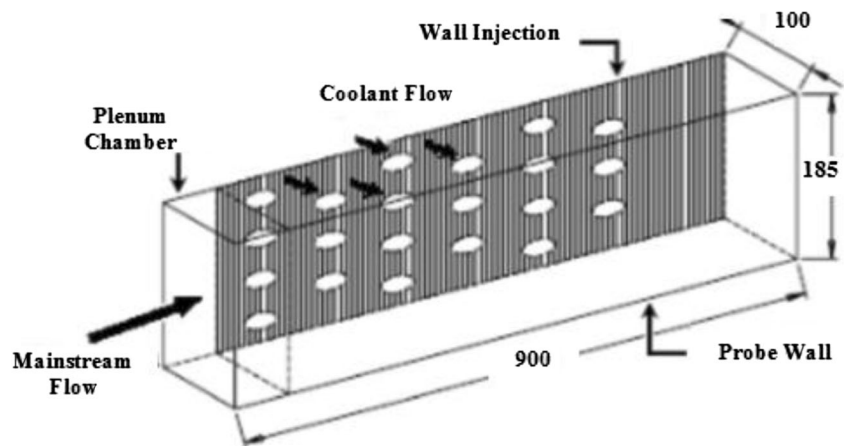
blades, an experimental apparatus is designed and realized in the LET laboratory (Laboratory for thermal studies) ENSMA in Poitiers. It is essentially made of a flat plate over which a main stream of air flows and it interacts with secondary flows coming from several rows of holes arranged in a staggered manner in the flat plate. The apparatus is instrumented with a PIV system for velocity measurements (Fig. 7). It encompasses several components that are:

1. MEIDINGER fan, type HP 98 / 10–13 20,000 Pa, to generate the main flow.
2. Test vein carrying a multi perforated wall of 81 holes, their angles are 30° from the wall and have 6 mm in diameter.
3. Instant image acquisition camera.
4. Laser beam generator to illuminate the study area.
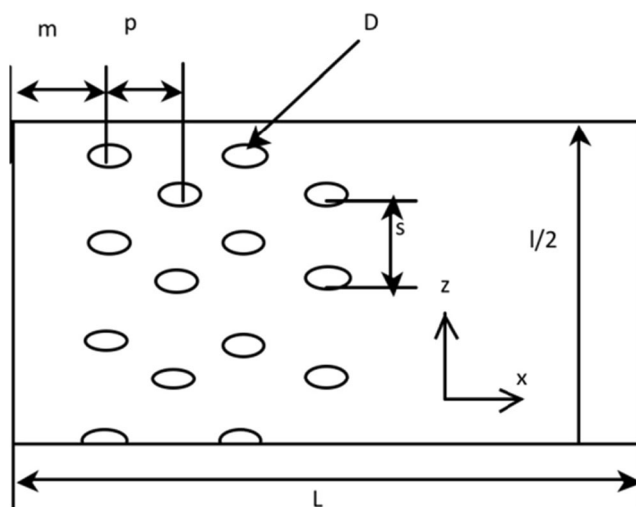5. Flow control valve.

Fig. 4 Geometrical distribution of the holes

3.1 Flow rate and speed measurement system

The first flow control system which is situated upstream of the test vein is a valve (Fig. 7), it measures the flow rate of the main flow Q_e. The second one (not shown in the figure) placed downstream of the test stream measures the flow rate of the flow sucked by the depressor Q_d (therefore the flow rate of the injection flow Q_i). The mass flow rate of each flow is regulated and measured by a flow control system. Each flow control system consists of a venturi for measuring the flow rate and an adjustment valve for setting a desired flow rate. The venturi is connected to absolute and differential pressure sensors to measure the velocities of the air flow. For all the experiments carried out, the mass flow rate of the main flow was fixed at 45 g.s^{-1}, so that the injection flow can reach a maximum of 25 g.s^{-1}.

3.2 Aerodynamic conditions

The essential aerodynamic condition taken into account in this experiment is the injection rate M, calculated according to the following formula:
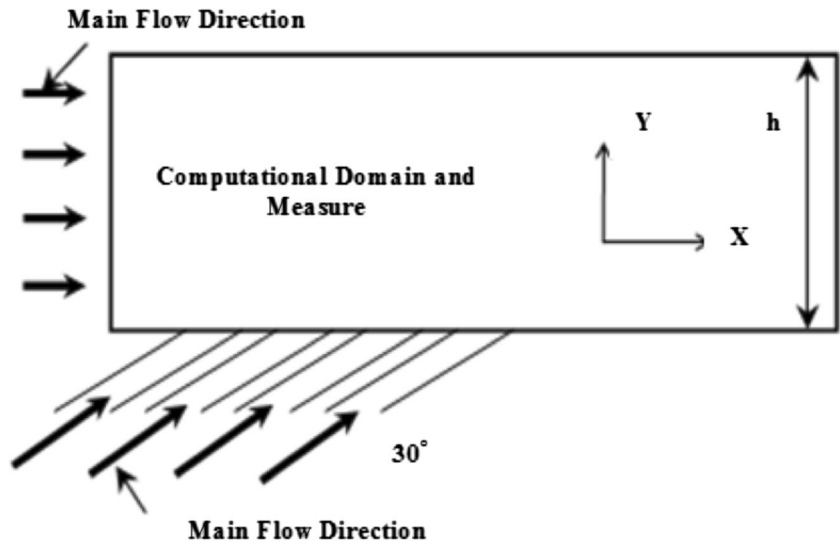
$$M = \frac{\rho_i U_i}{\rho_e U_e} \tag{1}$$

Where;

ρ_e, U_e, U_i and ρ_i represent respectively the main flow density, the main flow velocity, the injection flow velocity and the jet density flow.

The injection rate M can also be written in the following form

$$M = \frac{\rho_i U_i (nS_i)}{\rho_e U_e S_e} \times \frac{S_e}{nS_i} \tag{2}$$

Fig. 5 Calculation domain and experimental setup

Where S_i is the injection area which is calculated by

$$S_i = \frac{\pi D^2}{4} \tag{3}$$

Where

S_e represents the tunnel test section ($S_e = 0{,}0185$ m^2)
n is the open injections number

The main mass flow rate and of the injection flow rate are calculated by the relations below

$$Q_e = \rho_e U_e S_e \tag{4}$$

$$Q_i = \rho_i U_i (n S_i) \tag{5}$$

From these formulas, a relationship can be deduced between the injection rate M and the flow rates of the main flow Q_e and the injected air Q_i

$$M = K \frac{Q_i}{Q_e} \ , \quad K = \frac{S_e}{n S_i} \tag{6}$$

Q_i is the mass flow rate of the injection flow (kg.s^{-1})
Q_e is the mass flow rate of the main flow (kg. s^{-1})

For all the configurations studied, the main mass flow rate is fixed at 45 g.s^{-1} which corresponds to the mean flow velocity of 2 m.s^{-1}. The blowing flow rate M has been therefore controlled by the mass flow rate of the injection flow.
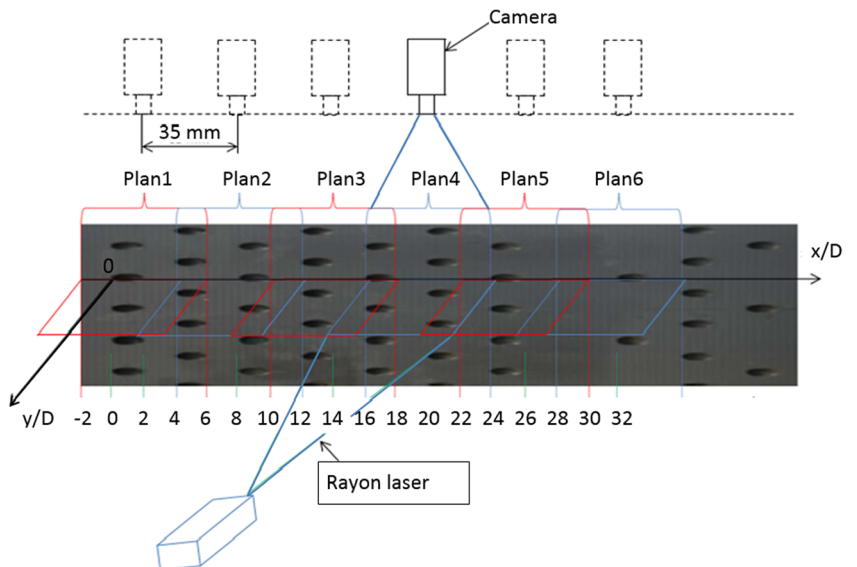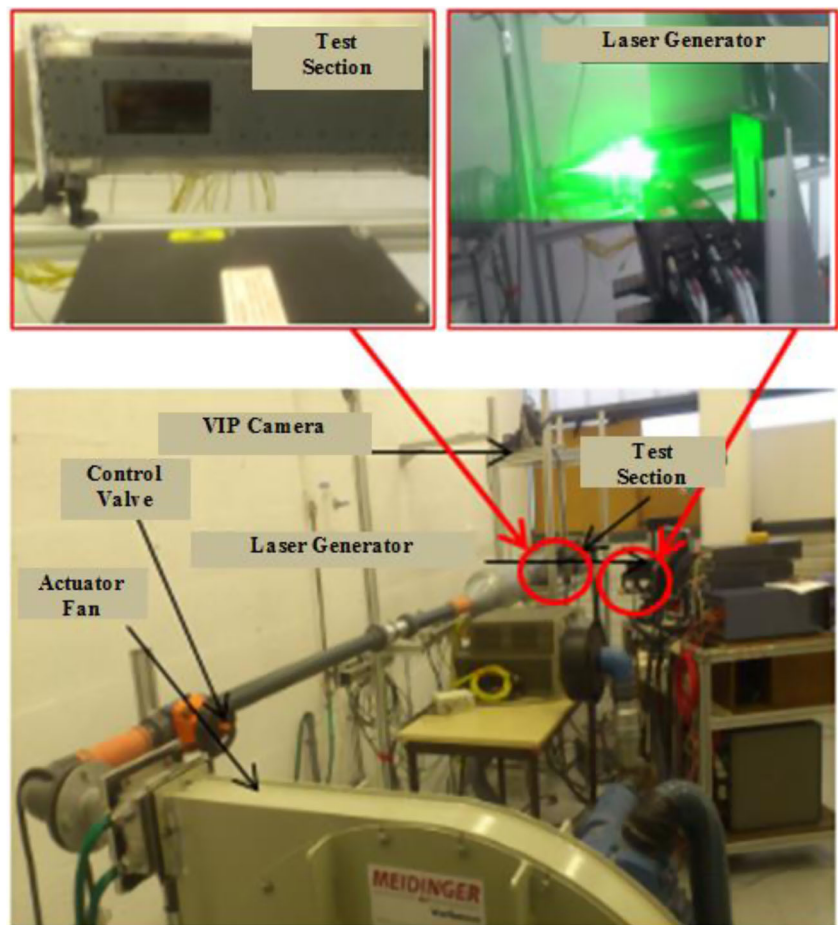
Fig. 6 Measurement plans available with PIV

Fig. 7 Experimental apparatus

4 Mathematical formulation

CFD analysis work has been performed in order to validate the CFD model including selection of the turbulence model, specifying adequate inlet conditions, evaluation of the grid dependence, etc. At that, among other data of practical interest, the local heat transfer is most sensitive to peculiarities of secondary flows and, consequently, to details of physical and computational modelling. The Navier-Stokes equations governing the fluid flows are given below:

$$\frac{\partial \overline{\rho u_i}}{\partial x_j} = 0 \qquad \overline{u}_j \frac{\partial \overline{\rho u_i}}{\partial x_j} = \\ -\frac{\partial \overline{p}}{\partial x_i} + \frac{\partial}{\partial x_j}\left[\rho\nu\left(\frac{\partial \overline{u}_i}{\partial x_j} + \frac{\partial \overline{u}_j}{\partial x_i}\right) - \rho\overline{u_i' u_j'}\right] \qquad (7)$$

Where $-\rho\overline{u_i' u_j'}$ are the Reynolds turbulent stresses.

4.1 Standard k-ε model

In the standard k-ε model, the Reynolds stresses are modelled as:

$$-\rho\overline{u_i' u_j'} = -\frac{2}{3}\rho k \delta_{ij} + 2\mu_t \overline{S}_{ij} \qquad (8)$$

The eddy viscosity μ_t is related to the turbulent kinetic energy k and to its dissipation rate ε as:

$$\mu_t = \rho C_\mu \frac{k^2}{\varepsilon} \qquad (9)$$

Equation (8) represents a linear relationship between the turbulent stress and the strain rate, and forms the basis for all linear two-equation models. Distributions of k and ε in the flow field are determined from their modelled transport equations. The source terms in the modelled equations are given by:

$$S_k = P-\varepsilon; \quad S_\varepsilon = S_{\epsilon 1}\frac{\varepsilon}{k}P - C_{\epsilon 2}\frac{\varepsilon^2}{k} \qquad (10)$$

Where P is the production of turbulence

$$P = -\rho\overline{u_i' u_j'}\frac{\partial \overline{u}_i}{\partial x_j} \qquad (11)$$

For the turbulence, kinetic energy, a zero value is specified at the wall, while the value of dissipation at a near wall point is set, using a local equilibrium assumption, as

$$\varepsilon = C_\mu^{3/4} \frac{k^{3/2}}{0.4 \, \delta \, y} \tag{12}$$

4.2 SST model

Menter [18] combines the k-ε and k-ω models in a way that would allow them to be used in the regions where they show best advantages. In other words, the method uses the k-ω model near the wall, but switches through a function F1 to the k-ε equations away from the wall, these equations having been transformed to a k-ω format. He calls this model as shear stress transport. The final equations are:

$$\frac{\partial}{\partial t}(\rho k) + \overline{u}_j \frac{\partial}{\partial x_j}(\rho k) = \tau_{ij} \frac{\partial \overline{u}}{\partial x_j} - \beta^* \rho \omega k$$
$$+ \frac{\partial}{\partial x_j}\left[(\mu + \sigma_k \mu_t)\frac{\partial k}{\partial x_j}\right] \tag{13}$$

$$\frac{\partial}{\partial t}(\rho \omega) + \overline{u}_j \frac{\partial}{\partial x_j}(\rho \omega) = \frac{\mu}{\mu_t}\tau_{ij}\frac{\partial \overline{u}}{\partial x_j} - \beta \rho \omega^2$$
$$+ \frac{\partial}{\partial x_j}\left[(\mu + \sigma_\omega \mu_t)\frac{\partial \omega}{\partial x_j}\right] + 2(1 - F_1)\rho \sigma_{\omega 2}\frac{1}{\omega}\frac{\partial k}{\partial x_i}\frac{\partial \omega}{\partial x_j} \tag{14}$$

The constants in the SST model are calculated as follow. If ϕ is the constant in the SST model and ϕ_1 and ϕ_2 are the constants in the k-ω model and the transformed k-ε model, respectively, then

$$\phi = F_1 \phi_1 + (1 - F_1)\phi_2 \tag{15}$$

The constants in the k-ω are:
$\sigma_{k1} = 0{,}85$, $\sigma_{\omega 1} = 0{,}5$, $\beta_1 = 0{,}075$, $a_1 = 0{,}31$, $\beta^* = 0{,}09$, K = 0{,}41,

$$\gamma_1 = \frac{\beta_1}{\beta^*} - \frac{\sigma_{\omega 1}K^2}{\sqrt{\beta^*}} \tag{16}$$

The constants in the transformed k-ε model are:
$\sigma_{k2} = 1{,}0$, $\sigma_{\omega 2} = 0{,}856$, $\beta_2 = 0{,}0828$, $\beta^* = 0{,}09$, K = 0{,}41,

$$\gamma_1 = \frac{\beta_2}{\beta^*} - \frac{\sigma_{\omega 2}K^2}{\sqrt{\beta^*}} \tag{17}$$

$$-\rho \overline{u_i' u_j'} = -\frac{2}{3}\rho k \delta_{ij} + \mu_t \left(\frac{\partial \overline{u}_i}{\partial x_j} + \frac{\partial \overline{u}_j}{\partial x_i}\right) \tag{18}$$

$$F_1 = \tanh\left(\arg_1^4\right) \tag{19}$$

$$\arg_1 = \min\left[\max\left(\frac{\sqrt{k}}{0.09\,\omega\,y}, \frac{500\,\nu}{y^2\,\omega}\right), \frac{4\,\rho\,\sigma_{\omega 2}k}{CD_{k\omega}y^2}\right] \tag{20}$$

$$CD_{k\omega} = \max\left(2\,\rho\,\sigma_{\omega 2}\frac{1}{\omega}\frac{\partial k}{\partial x_j}\frac{\partial \omega}{\partial x_i}, \, 10^{-10}\right) \tag{21}$$

$$\nu_t = \frac{a_1 k}{\max\left(a_1\,\omega, \Omega\,F_1\right)} \tag{22}$$

$$F_2 = \tanh\left(\arg_2^4\right) \tag{23}$$

$$\arg_2 = \max\left(2\frac{\sqrt{k}}{0.09\,\omega\,y}, \frac{500\,\nu}{y^2\,\omega}\right). \tag{24}$$

4.3 Reynolds stress model (RSM)

The Reynolds stress models (RSM) also known as the Reynolds stress transport (RST) models, are of a higher level. In this model the Reynolds stresses $\rho \overline{u_i' u_j'}$ are calculated according to their own transport equations and the concept of (isotropic) turbulent viscosity is not required. So this model involves the individual calculation of each stresses. These equations are used to obtain a closure of the Reynolds averaged equations system for the transport of the momentum. The method of closure employed is usually called a second order closure. This modelling approach is from the work of [Launder (1975)]. In RSM, the eddy viscosity approach has been discarded and the Reynolds stresses are directly computed. The exact Reynolds stress transport equation accounts for the directional effects of the Reynolds stress fields. The exact transport equations for the transport of the Reynolds stresses, $\overline{u_1' u_j'}$, may be written as follows:

$$\frac{\partial}{\partial t}\left(\rho \overline{u_i' u_J'}\right) + \frac{\partial}{\partial x_k}\left(\rho u_k \overline{u_J' u_i'}\right) = -\frac{\partial}{\partial x_k}\left[\rho \overline{u_i' u_J' u_k'} + \overline{p'\left(\delta_{kJ}u_i' + \delta_{1k}u_J'\right)}\right]$$
$$+ \frac{\partial}{\partial x_k}\left[\mu \frac{\partial}{\partial x_k}\left(\overline{u_i' u_J'}\right)\right] - \rho\left(\overline{u_i' u_k'}\frac{\partial u_j}{\partial x_k} + \overline{u_J' u_k'}\frac{\partial u_i}{\partial x_k}\right)$$
$$- \rho \beta\left(g_i \overline{u_J'\theta} + g_j \overline{u_1'\theta}\right) + \overline{p'\left(\frac{\partial u_i'}{\partial x_j} + \frac{\partial u_j'}{\partial x_i}\right)} - 2\mu \overline{\frac{\partial u_i'}{\partial x_k}\frac{\partial u_j'}{\partial x_k}}$$
$$- 2\rho \Omega_k\left(\overline{u_J' u_m'}\varepsilon_{ikm} + \overline{u_1' u_m'}\varepsilon_{jkm}\right) + S_{user} \tag{25}$$

Local Time Derivate $C_{ij} = D_{Tij} + D_{Lij} + P_{ij} + G_{ij} + \varnothing_{ij} - \varepsilon_{ij} + F_{ij} +$ User-Defined Source Term where C_{ij} is the Convection-Term, equals the Turbulent Diffusion, D_{Lij} stands for the Molecular Diffusion, P_{ij} is the term for Stress Production, G_{ij} equals Buoyancy Production, $\varnothing_{ij}$ is for the Pressure Strain, ε_{ij} stands for the Dissipation and F_{ij} is the Production by System Rotation.

Of these terms C_{ij}, D_{Lij}, P_{ij} and F_{ij} and do not require modeling. After all, D_{Tij}, G_{ij}, $\varnothing_{ij}$ and ε_{ij} have to be modeled for closing the equations.

The Reynolds stress tensor, $\rho \overline{u_1' u_J'}$, is usually anisotropic. So, the second and third invariances of the Reynolds-stress

anisotropic tensor b_{ij} are nontrivial, in which $b_{ij} = \frac{\overline{u'_i u'_j}}{2k}_J - \frac{\delta_{ij}}{\varepsilon}$ and equal to $\frac{\overline{u'_i u'_j}}{2}$. It is naturally to suppose that the anisotropy of the Reynolds-stress tensor results from the anisotropy nature of turbulent production, dissipation, transport, pressure-stain-rate, and the viscous diffusive tensors. Such a correlation is described by the Reynolds stress transport equation. Based on these consideration, a number of turbulent models, such as Rotta's model and Lumley's return-to-isotropy model, have been established. Rotta's model describes the linear return-to-isotropy behavior of a low Reynolds number homogenous turbulence in which the turbulent production, transport, and rapid pressure-strain-rate are negligible. The turbulence dissipation and slow pressure-strain-rate are preponderant. Under these circumstance, Rotta suggested $\frac{db_{ij}}{dt} = -(C_R - 1)\frac{db_{ij}}{dt}b_{ij}$. Here, C_R is called the Rotta constant.

The constants suggested for use in this model are as follows:

$C_s \approx 0,25, C_1 \approx 0,25, C_\gamma \approx 0,25$

4.4 Near-wall treatment

A much better relation used is the law of the wake developed by Don Coles [19] and coupled with the universal law of the wall. In this approach the velocity profile is normalized by the wall friction velocity.

$$y^+ = \frac{yu^*}{\nu} \qquad (26)$$

Where $u^* = \sqrt{\frac{\tau_w}{\rho}}$ is the Friction velocity and $\tau_w = \mu \frac{\partial U}{\partial y}\Big]_{y=0}$ is the wall shear stress.

When the RSM model is used, near the walls Fluent applies explicit boundary conditions for Reynolds stresses using the logarithmic law, assuming steady state and neglecting convection and diffusion in the stress transport equation. Using a local coordinates system and on the basis of experimental results, near the walls we have: $\frac{\overline{u_t^2}}{k} = 1,098$.

4.5 Computational domain and boundary conditions

Figure 8 shows the three-dimensional numerical flow domain represented by the symmetrical plane which is the same at the ISAE-ENSMA test facility. Four staggered rows of cylindrical cooling hole section of 6 mm diameter and 4 as the value of the hole spacing ratio were located on the flat plate. The hole spacing ratio in the transverse direction s/D, is 4 and in the axial direction p/D is 4. The modeled transport equations are solved using a three-dimensional using the commercial

computational fluid dynamics code FLUENT. The calculation domain and boundary conditions taken for the numerical simulations and experiments are shown in Fig. 8. The second-order upwind scheme has been used for the discretization. In the case of the film cooling, both the cross flow and cooling jet fluids are in general the ambient air. The low temperature and pressure levels considered in this work are such that the air is considered as a perfect gas in the macroscopic sense. The dimensions of the experimental study (real) and numerical case are given in Table 1.

The elliptical partial differential equations nature requires boundary conditions in all boundaries. It was therefore considered in a special way in the present work, three types of boundary conditions, as shown in the Fig. 8. These three types are:

velocity inlet: outflow and symmetry.

α is the jet penetration angle = 30°
D is the slot width = 0,006 m

One major step in simulating fluid flows with turbulence model is the choice of appropriate inlet values of the solved primary variables u, v, k, ε or ω for the flow entering the computational domain. The boundary conditions are derived from the experimental measurements [3]. On the jet exit surface, the axial and the vertical velocity components are defined, while the lateral velocity is being neglected. In the upstream boundary, the axial velocity profile, profiles are also specified. The axial velocity component is given in the external flow, while the kinetic turbulent energy and the dissipation rate are calculated. The upstream and downstream conditions have zero gradients for all the state variables.

5 Numerical method

The standard wall-function approach [19] is used to specify the wall boundary conditions for velocity. For a turbulent
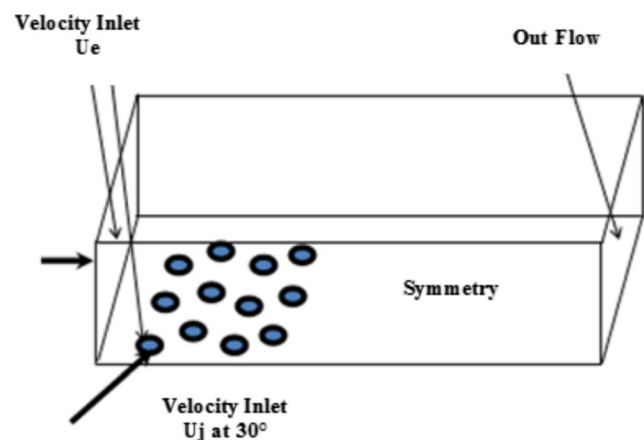

Fig. 8 Experimental and numerical studies: 3-D domain and boundary conditions

boundary layer on a smooth flat plate, the correlation is valid for Re < 10^9. The density and viscosity for air are measured at sea-level: often it be considered T_{20} = 293,15 K (20 °C), where ρ_{20} = 1204 kg.m^{-3} and ν_{20} = 1,71.10^{-5} m^2.s^{-1} (μ = 1,79.10^{-5} kg.m^{-1} s^{-1}). Applied to the incompressible studied flow, it is then able to estimate y + for the corresponding grids. Results are presented in Table 1.

Figure 9 shows a comparison between a coarse mesh, a medium and a fine mesh. The results show the appearance of the reduced axial mean velocity profiles U/Ue obtained by the turbulence model k-ε in the station x/D = 0 for three different meshes; coarse mesh (557,381 cells), medium mesh (1,682,849 cells), and fine mesh (2,575,565 cells), This study was conducted to see the effect of the mesh on the obtained results, in order to select a suitable mesh (which gives good results with minimum possible number of nodes to gain CPU time calculation). We note that the reduced velocities are almost the same for the medium and the fine mesh. So, we preferred to use a medium for all the calculations.

The modeled transport equations were solved using a three-dimensional CFD FLUENT code based on the SIMPLEC algorithm. The second-order upwind scheme has been used for the discretization.

6 Results and discussion

6.1 Results analysis

In the present work, representative results of time-averaged flow field obtained with the particle-image velocimetry (PIV) measurements and RANS studies are compared with a focus on determining the predictive capabilities of numerical method. FLUENT code is used to solve turbulent flow over a flat plate to determine the best turbulence model to use. Boundary conditions were: U_{inlet} = 2 m/s, T_{inlet} = 300 K, T_{plate} = 400 K, Tu_i = 1%. Three two-equation turbulence models, Standard k-ε, RSM and SST are used. The discussion of the results consists of a comparison of numerical
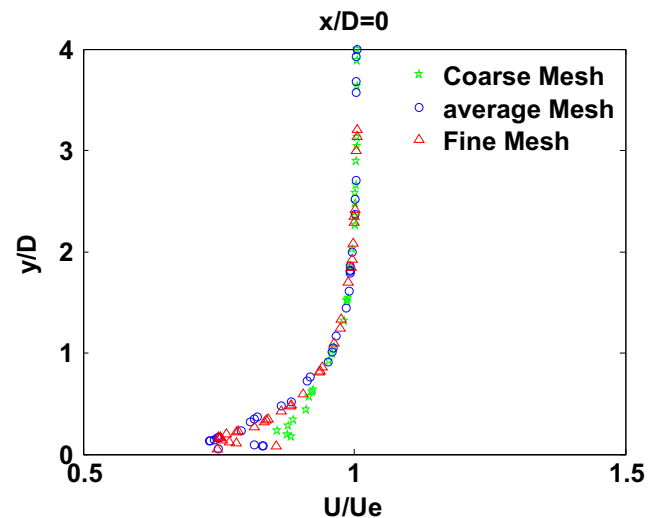

Fig. 9 Comparison between axial reduced velocities U/Ue obtained by the turbulence model k-ε with a fine mesh, medium mesh and a coarse mesh

calculations with experimental data to show the quality of the computational method. Then the exit jets area and the spreading are investigated, and the mixing process is analyzed. To obtain the mean and the time-averaged quantities, the flow field has been sampled over six combined stream wise and span wise planes. Here, one of the combined planes corresponds to one measure. So, six measures have been conducted for that the cross flow fluid needs to pass over the complete measurement domain which contains the six planes.

6.2 Flow calculation results

6.2.1 Reduced axial and vertical velocity: comparison between the experiments

To visualize the flow interaction behavior of the jet entering the cross flow, simulations of mean and turbulent velocity profiles of flow over a flat plate are plotted at the x − z baseline (center plane) in Figs. 10 and 11 in comparison with the measured quantities. The main objective here is to discuss how the

Table 1 Grid spacing computation for a given Y+

|	Incompressible flow for experimental study	Compressible flow for numerical study
U_e (m/s)	2.0	248.0
L (m)	0.90	0.25
Re_C	$1.2\ 10^5$	$4.13.\ 10^6$
Y+	10.0	10.0
Y_w (m)	0.00151	$16.\ 10^{-6}$
Length (m)	0.9	0.9
Width (m)	0.1	0.1
Height(m)	0.185	0.185

Fig. 10 Comparison between measured and calculated of reduced average velocities (U/Ue) along the center plane Z/D = 0
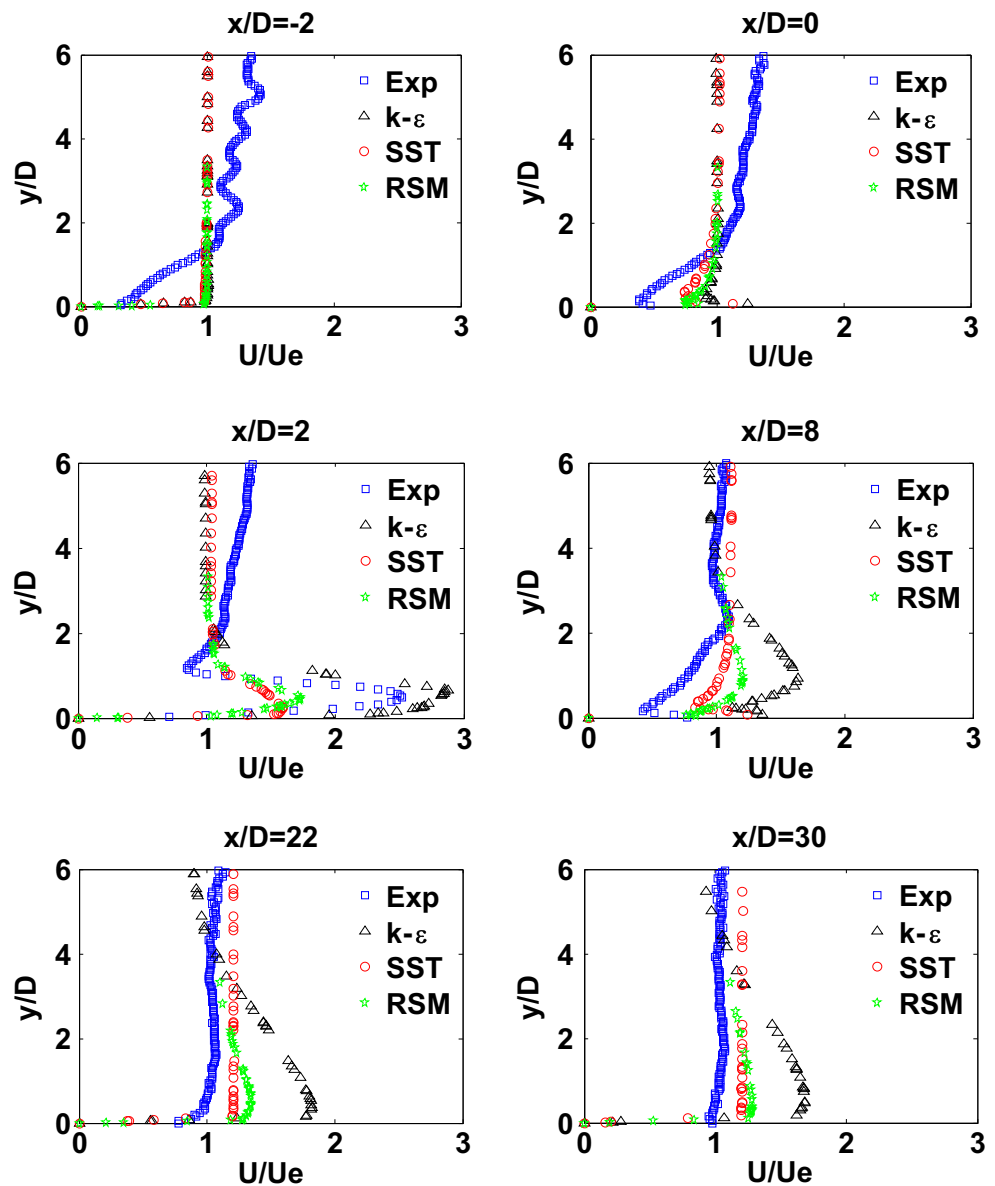
three models are in agreement with experimental results and how to provide the best behavior of the flows interaction, since the jets exit into cross flow until far downstream. The Figures show the comparison between the PIV measurements and the three-dimensional calculation results on flat plate obtained for the three turbulence models used: the k-ε, the RSM and the SST and for the same blowing rate (M = 2). Some discrepancies are observed in the flow near the wall. The reduced axial velocity is, in general, over predicted by the three models in comparison with experiment. The axial U/Ue and vertical V/Ue reduced mean velocities component profiles are presented and discussed along the span wise symmetry plane (Z/D = 0) at different stream wise locations: X/D = − 2, x/D = 0, x/D = 2, x/D = 8, x/D = 22 and x/D = 30. The profile analysis shows that in the neighborhoods of the injection exit

area, the external flow is clearly disturbed deflected under the jet influence. Also, just behind the jets and over the wall, the results show strong differences between the three models compared with experience. The pressure side jets of the injection row are more directed and may leave only low effectiveness coolant traces along the end wall surface indicating that a high momentum flux is inducing jet lift off. The reduced axial velocity is over predicted by the three models in comparison with experiments (PIV). Nevertheless, RSM and SST models are the best to reproduce the behavior of experimental results. The over-prediction of the mean axial velocity may be explained by the ability of RSM and SST models to capture the energy production and transport associated with the coherent scales but over than shown by the experiments. The RSM predictions do not show any significant improvement over the

Fig. 11 Comparison between measured and calculated of reduced average velocities (V/Ue) along the center plane Z/D = 0
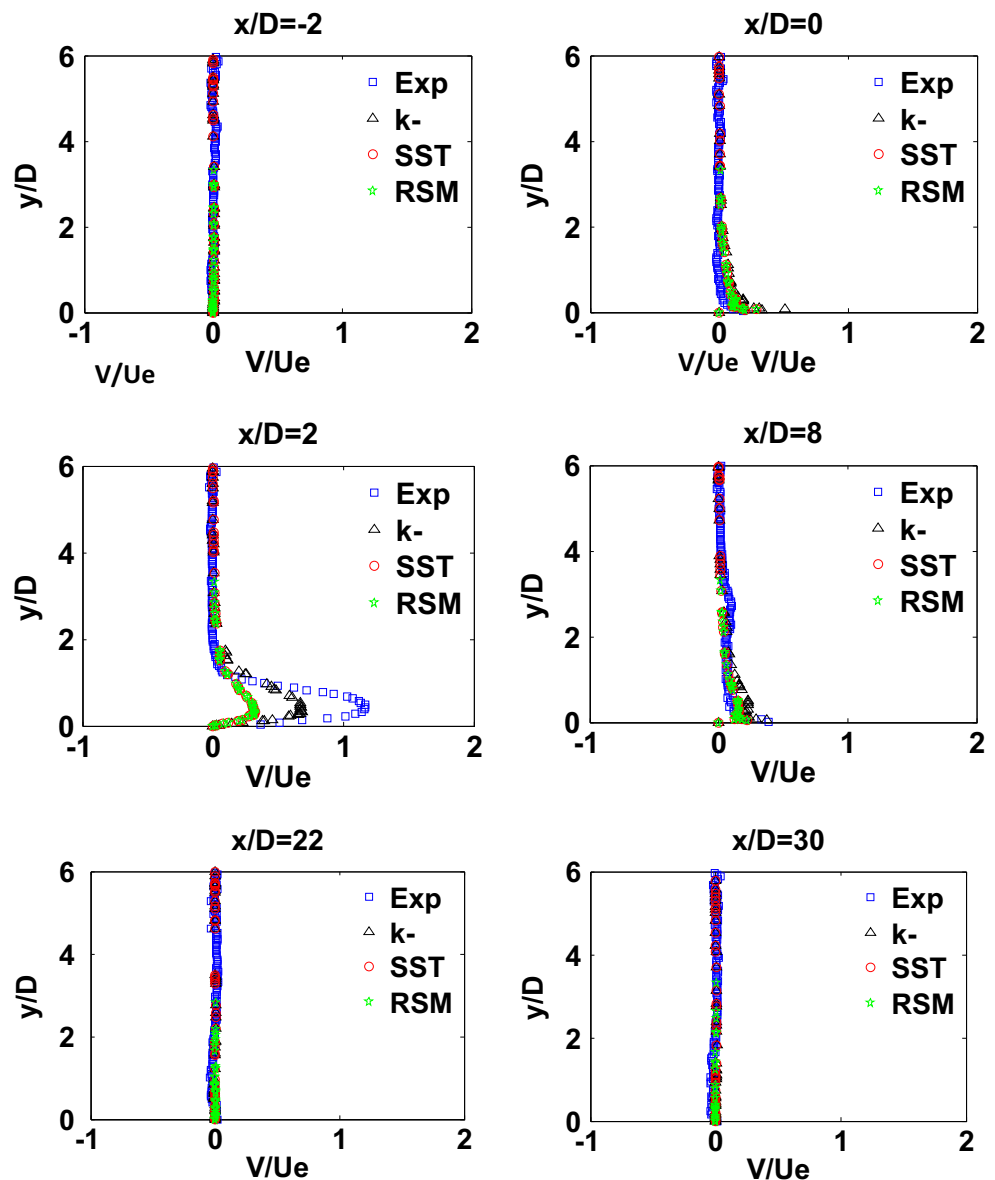
SST model. This can point to the fact that the anisotropy in the turbulent flow and the effects of the streamlines curvature are not the major contributor to the lack of agreement. Hence, the discrepancy may come from the inability of the RANS method to make the difference between large and low scales or the large-scale unsteadiness. The k-ε model seems to over predict the wake regions of the jet flows than showed by the experiment results and compared with the RSM and the SST model. This could be explained by the deficient of this model to be sensitive to some disturbed flow near the boundary layer, due to its isotropy formulation. Further downstream (X/D > 20), the jets appear to be largely unaffected because the mixing flow is fully developed. Furthermore, the comparison between the numerical results of SST, RSM and k-ε models with the experience (PIV) shows marked differences about the jets spreading. Indeed, all three models do not adequately

reproduce the spread evolution, which is larger in height than in length as shown by the experience. In the immediate injection area (X/D = − 2, x/D = 0, x/D = 2) the numerical results fail to capture quantitatively the experimental data because the anisotropy in the turbulent flow is the major contributor to the lack of agreement. So, the discrepancy may come from the inability of the RANS method to make a difference between large and low scales or the large-scale unsteadiness. Far from the injection area (x/D = 8, x/D = 22 and x/D = 30), this may be explained by the effect of some geometric parameters like the pitch between holes and like the planer angle. The area in the region between adjacent holes exposed to the mainstream is increased when the p/d is increased. Fortunately, the kinetic energy in local region is not dominant influential factor to produce some differences. Otherwise, the main reason is that it is considered that the mixing between the cooling air and the
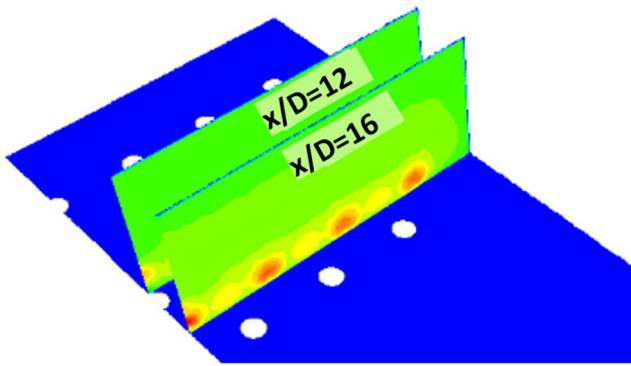
Fig. 12 Center planes X/D = 12 and X/D = 16

mainstream occurred mainly in a downstream region of the exit of film holes to cause different diffusing to two sides. So, this may be explain the differences showed between numerical and experiment results.

6.2.2 Contours lines of velocity magnitude: numerical results

To visualize the laterally spreading (Z/D direction) behavior, Fig. 12 shows the reduced mean velocities of the three-dimensional calculation jets-cross flow

interaction. Reduced velocity profiles are plotted at three stream wise positions x/D = 12 and 16 positions and along the span wise plane Z/D. Measurements by the PIV technic were not possible in the transverse planes because of the impossibility of moving and manipulating the camera, so only numerical results are presented and discussed for the three turbulence models. Results are presented and discussed in Fig. 13 regarding to the constant velocity lines which provide information about the laterally spreading film. It is clear that the two models k-ε and SST are quite similar in their prediction of the shapes and velocity contours intensities. It may be noted that; for example, when X / D = 16 the magnitude of U/Ue values vary from 1,57 to 4,70 for the SST model, from 1,56 to 4,67 for the k-ε model and from 2,35 to 4,70 for the RSM model.

The results relating to the profiles of the average longitudinal velocity profiles at different span wise locations Z/D = −4; 0; 6 and 12 are shown in Fig. 14. Here again, it is clear that the three models are quite similar in their prediction of the jets exit into the main flow. The explanation of these phenomena was developed.

Fig. 13 Contours of velocities magnitude for k-ε, SST and RSM models in X/D = 12 and X/D = 16 center plane
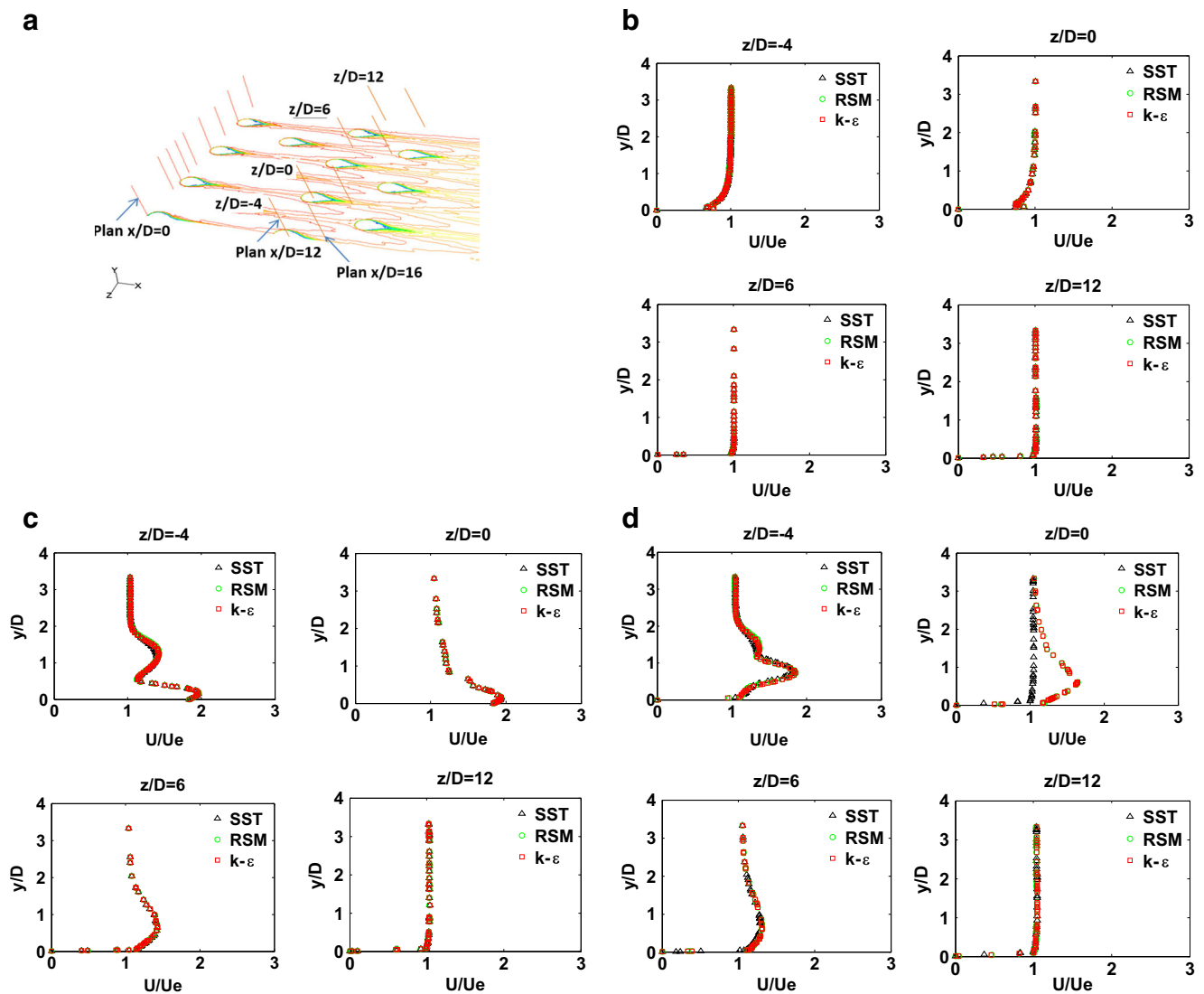
a

b

c

d
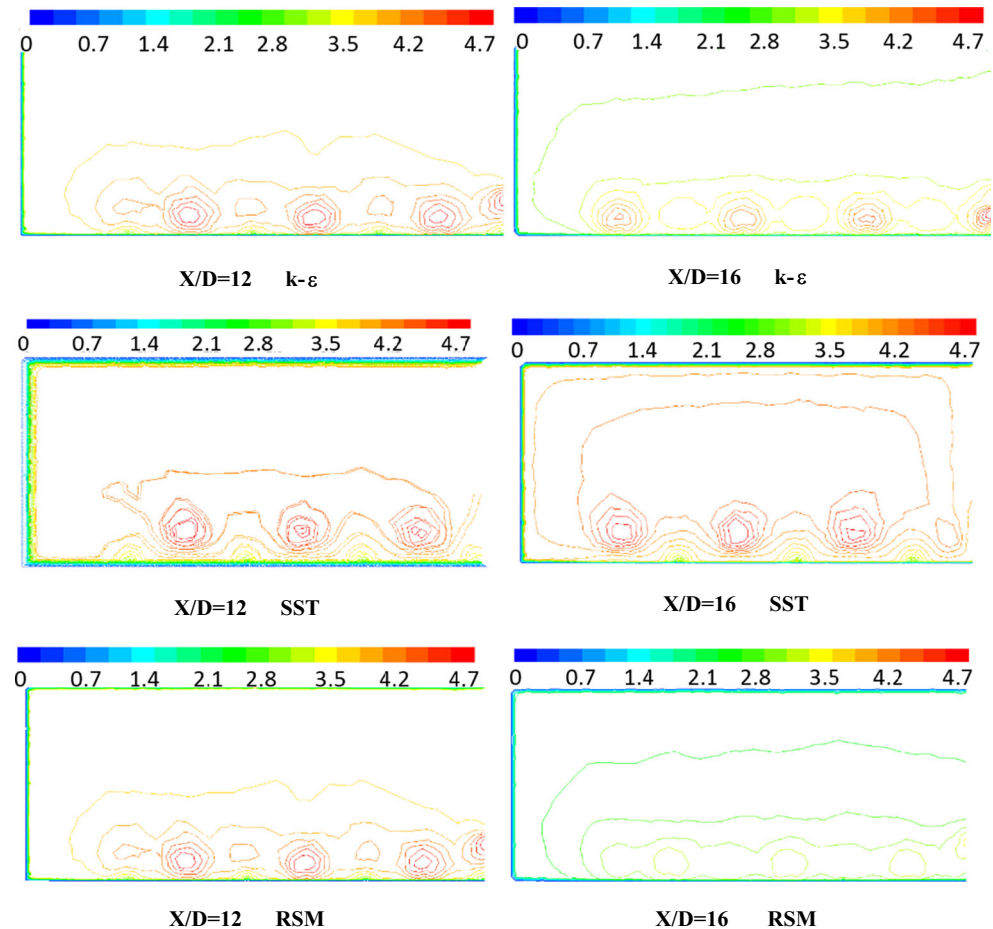
Fig. 14 Reduced average velocity profiles (U/Ue) obtained by k-ε, RSM and SST models. **a** Different span wise plane locations Z/D = −4; 0; 6 and 12 at different stream wise positions x/D = 0; 12 and 16. **b** Reduced average velocity profiles (U/Ue) obtained by k-ε, RSM and SST

models in X/D = 0. **c** Reduced average velocity profiles (U/Ue) obtained by k-ε, RSM and SST models in X/D = 12. **d** Reduced average velocity profiles (U/Ue) obtained by k-ε, RSM and SST models in X/D = 16

6.2.3 The turbulence kinetic energy along the jet center plane: comparison with the experiments

The turbulence kinetic energy evolution is shown in Fig. 15a, b, c, for the three turbulence models of Standard k-ε, RSM and SST, and compared with the experiments. Measurement results are shown in Fig. 15d and presented in the stream wise symmetrical plane Z / D = 0. The jets exit is well reproduced and their trajectory section is still visible at a vertical distance Y / D = 2 from the wall. The experimental result shows the well development of the jets path in interaction with the cross flow. Although two distinct regions are observed: the potential cone where kinetic energy of turbulence is very low (approximately 0.20 m² / s²) and section from the beginning of the path curvature of the jets under the influence of shear flow

transverse forces, where the kinetic energy of turbulence increases (1.5 m² / s² to 2.0 m² / s²) at Y / D = 2. The numerical result is reproduced relatively well compared with the experiment, especially far over the wall and from Y / D = 2. However, the comparison with the experiments results let in general, the appearance of some discrepancies between the numerical and experimental results.

7 Conclusion

RANS with three turbulence models is applied to simulate the entering and the spreading development of a cooling jet into a turbulent cross flow. The flow physics is discussed by identifying the development of the mixture mechanisms between

Fig. 15 Stream wise visualizations of turbulent kinetic. **a** Stream wise visualizations of turbulent kinetic energy obtained with k-ε model. **b** Stream wise visualizations of turbulent kinetic energy obtained with SST model. **c** Stream wise visualizations of turbulent kinetic energy obtained with RSM model. **d** Stream wise visualizations of turbulent kinetic energy obtained with PIV measurements
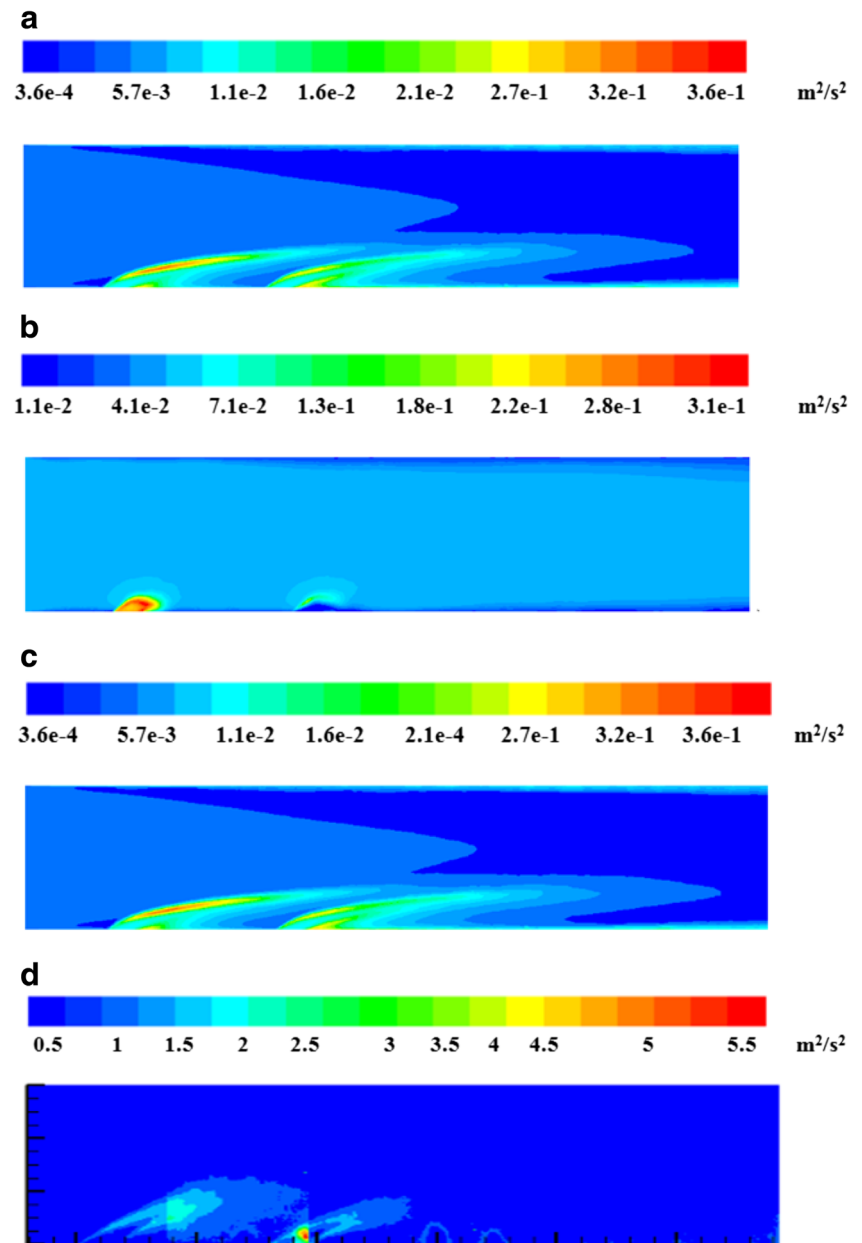
the jets of different rows. The time-averaged RANS predictions in terms of the turbulent kinetic energy are not in excellent agreement with experimental data, measured in this work. The flow physics is also discussed with the vortical structures results observed in the stream wise symmetric plane. A detailed analysis of the curvature effect proves the significance of the surface curvature in the dynamic flow field on the mixing process. Higher irregularity pattern of velocity profiles close to the wall may be attributed to the curvature effect than the predicted capability of each model. Any significant improvements are observed with the k-ε predictions in comparison with the SST and RSM models. The anisotropy in the flow turbulence and the effects of the surface curvature are not the major contributor to the lack of agreement and the

discrepancy may be provided from the inability of the RANS method to make a difference between large and low scales or the large-scale unsteadiness.

To summarize, the novelty of this work is to evaluate, using measurements by the PIV technic, the prediction capability of complex physical phenomena in the film cooling interaction using three closure models. For this, the comparison of the numerical and experimental results shows sometimes marked differences in near-wall regions in the vicinity and far downstream of the jets. Therefore, the choice of the three turbulence models used here may not be judicious or the RANS method is not well adapted to this kind of problem. Its limitations due to the isotropic approach should be noted. Moreover, as discussed above, the meshes used and based on the available

computer hardware may appear insufficient and therefore cannot capture the complex mechanisms of the two streams interaction in the axial and the span wise directions of the mixing flow, in the presence of several rows of jets. It is apparent that the developed mathematical formulations of turbulence models are capable of representing the flow field. Predicting the flow field based on the three turbulence flow models used in this work introduces some inaccuracy. Reducing these inaccuracies particularly for the velocity components is the most prominent improvement opportunity of the current modeling.

References

1. Andreopoulos J, Rodi W (1984) Experimental investigation of jets in a cross-flow. J Fluid Mech 138:93–127
2. Fric TF, Roshko A (1989) Structure of Vorticity in the near field of the transverse jet. Tenth symposium on turbulent shear flows. Oxford University, Oxford
3. Dizene R (1993) Etude Expérimentale d'interaction de Jets avec un Ecoulement Transversal Compressible. Deuxième partie: Rangée de Jets Obliques. Thèse, CEAT, Université de Poitiers France
4. Ince NZ, Leschziner MA (1993) Comparison of three-dimensional jets in cross flow with and without impingement using reynolds stress transport closure. AGARD symposium on computational and experimental assessment of jets in crossflow
5. Demuren AO (1994) Modelling jets in cross flow, NASA Contractor Report 194965, ICASE. Report N°94–71, Contract NAS1–19480
6. Sen B, Schmidt DL, Bogard DG (1996) Film cooling with compound angle holes. Heat Transfer ASME J of Turbomachinery 118: 800–806
7. Schmidt DL, Sen B, Bogard DG (1996) Film cooling with compound angle holes: adiabatic effectiveness. ASME J of Turbomachinery 118:807–813
8. Cho, H. H., Kim, B. G., Rhee, D. H, [1998], Effects of Hole Geometry on Heat (Mass)Transfer and Film Cooling E®ectiveness. Proceedings of 11th IHTC, Kyongju, Korea.
9. Yuen CHN, Martinez-Botas RF (2003) Film cooling characteristics of a single round hole at various stream wise angles in a cross flow. Part I effectiveness. Int J Heat Mass Transf 46:221–235
10. Gritsch M, Schulz A, Wittig S (1998) Adiabatic Wall effectiveness measurements of film-cooling holes with expanded exits. J Turbomach 120(3):549–556. doi:10.1115/1.2841752 History
11. Tyagi M, Acharya S (2003) Large eddy simulation of an inclined film cooling Jet 125:734–742
12. Guo et al (2004) Large-Eddy simulation of a jet in a crossflow. Volume 9 of the series ERCOFTAC. Series pp 603–610
13. Leedom D.H. (2009) Numerical Investigation of Film Cooling Fluid Flow and Heat Transfer using Large Eddy Simulations. B.S., Louisiana State University, May 2009.
14. Yao Y, Zhang J, Yang Y (2013) Numerical study on film cooling mechanism and characteristics of cylindrical holes with branched jet injections. Propulsion and Power Research 2(1):30–37
15. Balaji K et al (2016) Review of cooling effect on gas turbine blade. International conference on systems, science, control, communication, engineering and technology, vol 2. Karpagam Institute of Technology, Coimbatore, pp 478–482
16. Dey M, Prakhar J, Roy AK (2016) Numerical investigation of film cooling effectiveness in turbine blades. American Journal of Fluid Dynamics 6(1):20–26
17. Sun X, Peng W (2016) Effect of film cooling holes shape of helium turbine blades in HTGR, 24th international conference on nuclear engineering 2016; 6(1): 20–26, (2016) 24th international conference on nuclear engineering, Volume 3: thermal-hydraulics Charlotte, North Carolina, USA, June 26–30, 2016
18. Menter FR (1993) Zonal two equation k-ω turbulence models for aerodynamic flows. AIAA Paper 93–2906
19. Coles D (1956) he law of the wake in the turbulent boundary layer. J Fluid Mech 1:191–226. [Guggenheim. Aeronautical Lab., California Inst. Technology, Pasadena, CA]